JOURNAL OF SPACECRAFT AND ROCKETS
Vol. 30, No. 4, July–August 1993

Solution Strategy for Three-Dimensional Configurations at Hypersonic Speeds

K. James Weilmuenster* and Peter A. Gnoffo*
NASA Langley Research Center, Hampton, Virginia 23681

A procedure that reduces the memory requirements for computing the viscous flow over a modified Orbiter geometry at a hypersonic flight condition is presented. The Langley aerothermodynamic upwind relaxation algorithm (LAURA) code, that which incorporates a thermochemical nonequilibrium chemistry model, a finite rate catalytic wall boundary condition, and wall temperature distribution based on radiation equilibrium, is used in this study. In addition, the effect of choice of second-order flux formulations, eigenvalue limiter, and grid density on surface heating is investigated. The surface heating from a flowfield calculation at Mach number 22, altitude of 230,000 ft, and 40-deg angle of attack is compared with flight data from three Orbiter flights.

Nomenclature

a	=sound speed, ft/s
h	=altitude, ft
M	=Mach number
$N_{Re\text{-cell}}$	=cell Reynolds number
P	=pressure, lb/ff^2
q	=heat flux, Btu/ft^2-s
T	=temperature, °R
V	=velocity, ft/s
x	=distance along yaw axis, in.
y	=distance along pitch axis, in.
z	=distance along longitudinal axis, in.
ε	=emissivity or eigenvalue limiter
ζ	=parametric coordinate
η	=parametric coordinate
μ	=eigenvector
υ	=viscosity, lb-s/ft^2
ρ	=density
σ	=Stefan-Boltzmann constant, Btu/ft^2-s°R^4

Subscripts

w	=wall value
0	=reference value
∞	=freestream value

Introduction

OVER the past decade, computational fluid dynamics (CFD) has become recognized as a legitimate tool for determining the aerothermodynamic environment for blunt entry shapes at hypersonic speeds. As an example, the aeroassist flight experiment (AFE) vehicle aerodynamics[1,2] and heating[3,4] at flight conditions have been determined by CFD methods. The resources required for the most complete of these solutions, i.e., complete three-dimensional, viscous, nonequilibrium chemistry, including base flow, exceed that of all but the largest supercomputers.

The application of CFD to the aerothermodynamic analysis of large winged entry configurations, such as the Space Shuttle and the HL-20, has lagged largely because of limited computational power and memory of available computer hardware. These vehicles enter the atmosphere at relatively high angles of attack, which will lead to one of two classes of problems (see Fig. 1). At moderate angles of attack, the subsonic portion of the flow is generally confined to the vehicle nose, although isolated pockets of subsonic flow can appear at the wing leading edge and tail. If the subsonic flow is confined to the vehicle's nose, numerous time-asymptotic methods have been developed to solve for the three-dimensional flowfield in this region. These solutions provide a data surface aft of the subsonic region from which spatial marching techniques can be used to continue the solution downstream. This method, which works well for both inviscid and viscous flows, is fast and requires relatively low computer storage. When the angle of attack is large (see Fig. 1), the subsonic region for inviscid flow is greatly expanded and can envelop most of the flowfield on the windward side of the vehicle. In this case, a time-asymptotic global solution technique is required to obtain a solution. Until the early supercomputers, such as the CDC STAR-100 and CRAY-1, became available, it was not practical to consider this type of solution for a complex three-dimensional shape; and, in their original configuration, the resources provided by these machines were marginal. It was not until multimegaword memory configurations of these machines became available that inviscid solutions having adequate resolution could be obtained for complex three-dimensional shapes.

In the early 1980s, Weilmuenster and Hamilton[5]—using the Space Shuttle configuration with a modified leeside geometry—made the first routine high angle-of-attack inviscid flow calculations about a winged entry vehicle and showed that computed surface pressures were in excellent agreement with Shuttle Orbiter flight data. In the late 1980s, generalized coordinate systems combined with upwind total variation diminishing (TVD) computa-

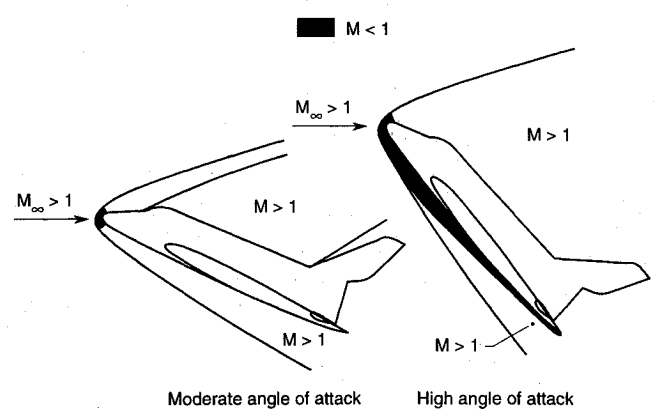

Fig. 1 Flowfields for supersonic/hypersonic flight regime.

Received June 26, 1992; presented as Paper 92-2921 at the AIAA 27th Thermophysics Conference, Nashville, TN, July 6–8, 1992; revision received Oct. 13, 1992; accepted for publication Oct. 16, 1992.

*Senior Research Engineer, Aerothermodynamics Branch, Space Systems Division.

tional schemes allowed the flow over geometrically complex configurations to be addressed using robust flow solvers. Greene et al.[6] have used these more recent developments to generate both perfect gas and equilibrium gas inviscid flowfield solutions about the HL-20. Also, Ma et al.[7] have shown that surface pressures obtained from inviscid Shuttle flowfield computations yielded vehicle aerodynamics which were in very good agreement with those given in the GRTLS aero data base. The cited inviscid solutions strain the practical limits of state-of-the-art supercomputers in terms of both computational power and CPU memory.

If inviscid solutions strain the limits of present day supercomputers, then viscous computations for complex three-dimensional configurations overwhelm these machines. Hamilton et al.[8] have obtained very good heat-transfer results for perfect gas solutions about a highly modified Shuttle configuration where the object was only to resolve the flow on the wind side of the vehicle. Even with this simplification, a single solution required 50 CRAY-2 hours and 60 megawords of CPU memory. Yamamoto[9] has recently reported on viscous, chemical nonequilibrium solutions for the HOPE vehicle.

The viscous solution techniques already cited are for either a perfect gas or for a gas in chemical equilibrium where the thermodynamic state of the gas is determined through the use of curve fits. They generate flowfield solutions that yield high quality surface pressure distributions[1,2,5] and when these solutions are coupled with approximate boundary-layer techniques[3,8] reasonable surface heating distributions can be determined. At flight conditions where nonequilibrium processes are important, there are no simple relations to describe the thermodynamic state of the gas and boundary-layer techniques are not available to determine surface heating. The only way to determine the surface pressures and heating at these conditions is through the solution of the viscous, nonequilibrium Navier-Stokes equations for a thermochemical nonequilibrium flow. Having to solve this complete set of equations greatly increases the computer resource requirements over those needed for a perfect gas, inviscid solution.

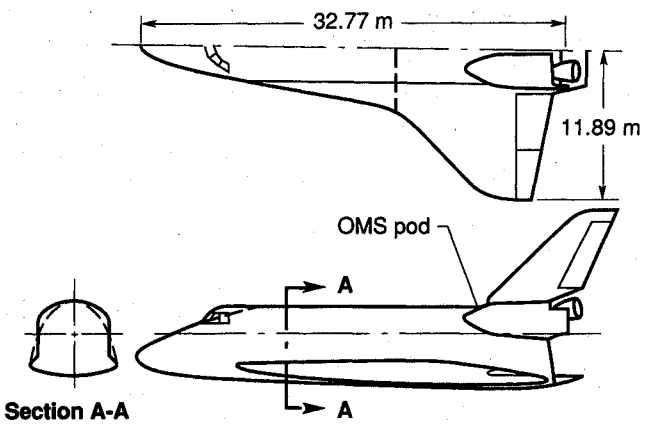

Fig. 2 Shuttle Orbiter geometry.

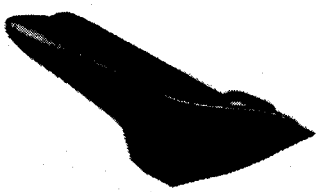

a) Complex geometry

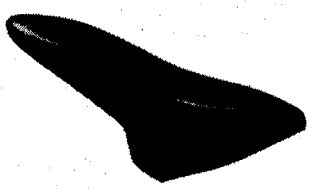

b) Modified geometry

Fig. 3 QUICK geometry models.

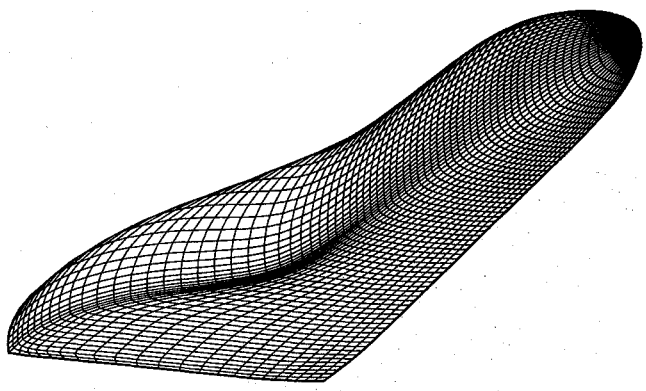

Fig. 4 Surface grid.

Present estimates of computer resources required for a viscous, chemical nonequilibrium solution for flow about the Shuttle Orbiter indicate resource requirements of up to 0.5 gigawords of memory and 500 CRAY-2 CPU hours. If flowfield solutions requiring resources of this magnitude are to be undertaken, several factors need to be considered. One factor to consider is how to structure such a large memory requirement problem so that it will fit within the memory of available hardware. A second factor, which is closely related to the first one, is the grid size required to properly resolve the flow about a complex three-dimensional configuration. In this paper, a segmented approach to determining solutions for these large problems will be demonstrated. In addition, the effect of grid resolution, TVD scheme, and eigenvalue limiter on surface heating will be shown along with comparisons to Shuttle Orbiter flight data.

Geometry Description

The vehicle configuration, a modified Shuttle Orbiter, used in this study has been the subject of several computational and experimental investigations.[5,8,10] The Space Shuttle Orbiter geometry is shown in Fig. 2.[11] Two versions of the geometry have been modeled with QUICK—a geometry description program—as shown in Fig. 3. The first (Fig. 3a) is a reasonably accurate model of the vehicle geometry with the vertical tail removed. The second (Fig. 3b) has the same lower surface shape and the same profile (except for the canopy) for the upper surface symmetry plane as the first, but has been modified by filling in the region between the leading edge of the strake or wing and the upper symmetry plane with elliptical segments as shown by the dashed lines in section A-A in Fig. 2. This process simplifies the leeside geometry and reduces the number of spanwise points required to describe the leeside geometry but does not effect the results obtained on the windward side because the inviscid crossflow velocity component goes supersonic near the leading edge of the strake or wing. Also, as shown in Fig. 3b, the surface definition used herein terminates at the elevon hinge line.

Surface and Volume Grid

An initial surface grid for the modified configuration shown in Fig. 3b was created using the QUICK geometry description. This grid was then used as the baseline surface definition in the GRIDGEN[12] grid generation system. Using GRIDGEN, grid points were redistributed on the surface, and a volume grid was constructed. A resulting surface grid consisting of 145 axial planes and 81 meridional planes is shown in Fig. 4. The volume grid with 41 points between the surface and outer boundary is shown in Fig. 5. For visual clarity, every other grid point is plotted in Figs. 4 and 5. The computational technique to be used will capture the bow shock,

Table 1 Freestream conditions

Flight	h, ft, $\times 10^5$	V, ft/s	ρ, slug/ft$^3 \times 10^6$	T, °R	P, lb/ft^2	M	Angle of attack, deg
STS-2	2.3	21,430	0.156	378	0.1014	22.47	39.8
STS-3	2.3	21,421	0.157	393	0.1062	22.03	40.0
STS-5	2.3	21,392	0.151	392	0.1026	22.02	39.9

thus the outer boundary of the volume grid has been constructed to ensure that it lies outside of the bow shock envelope. Adaption of the volume grid to the bow shock shape will be described in a later section.

Flight Data

During its first five flights, the Space Shuttle Orbiter was fitted with the developmental flight instrumentation (DFI) data acquisition system to record the surface pressures and temperatures on the vehicle during both the ascent and descent phases of flight. Although activated for all five flights, useful data are only available for the second, third, and fifth flights. A comparison of computed and measured windside surface pressures for these flights has been made in Ref. 5. Throckmorton et al.[13] used approximate computational techniques to create windward centerline heating distributions for comparison to this data, whereas Thompson[14] used a three-dimensional viscous-shock-layer technique and the same surface configuration used in this paper to make comparisons with flight data over a portion of the windward surface.

Throughout the five DFI flights, wall catalysis experiments were carried out using thermal protection tiles associated with individual thermocouple locations. Since these experiments significantly altered the measured wall temperatures and thus the wall heating, measurements from these locations have been excluded from the data base used in this paper. Details of the data reduction process used to generate surface heating data from measured surface temperatures as well as listings of the flight data for the surface heating and temperature for each of the three flights mentioned are given in Refs. 15–17. The DFI system consisted of a matrix of sensors covering the vehicle surface. The location and numerical identifier for each thermocouple located on the windward surface of the Shuttle Orbiter is shown in Fig. 6. Generally, the thermocouples are aligned along lines of constant axial distance or percentage of total span. Within a single grouping of gauges, for example, those at a constant span, the span location of each may vary slightly because of constraints on the location of a thermocouple within a thermal protection tile and the actual location of the tile on the vehicle surface.

Freestream Conditions

A single freestream condition was sought at which results of one CFD solution could be compared with the data from the flights of STS-2, STS-3, and STS-5. Since the surface heating is driven by the total energy in the freestream, which is proportional to $\rho_\infty V_\infty^3$, points along each flight trajectory with equivalent freestream velocity and density were identified. The freestream conditions given in Table 1 were chosen because at these conditions nonequilibrium effects in the flowfield would be important. Also, previous flight data analysis indicated that at these conditions, the flow over the entire lower surface of the vehicle was laminar.

Computational Technique

Code

The formulation of the Langley aerothermodynamic upwind relaxation algorithm (LAURA) is presented in detail in Refs. 18–20. The LAURA code as used here is set up for a three-dimensional, nonequilibrium air chemistry solution of the thin-layer Navier-Stokes equations. In the finite-volume solution algorithm, the inviscid first-order flux is constructed using Roe's flux difference splitting[21] and Harten's entropy fix[22] with second-order corrections based on Yee's symmetric total variation diminishing scheme.[23] In addition, computations also are made using the upwind total variation diminishing scheme described in Ref. 24.

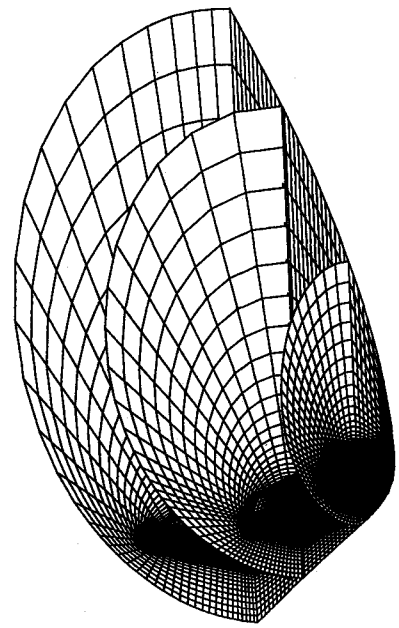

Fig. 5 Initial grid.

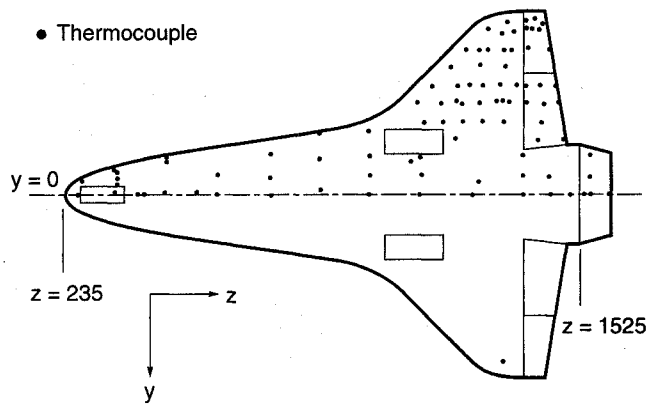

Fig. 6 Thermocouple locations on Orbiter lower surface.

Chemistry

A 7-species chemical reaction model is used in the code for these computations. The species N, O, N_2, O_2, NO, NO^+, and e^- are accounted for in the model

Boundary Conditions

The usual no-slip boundary condition for viscous flow is applied at the wall whereas freestream conditions are set at points on the outer boundary of the computational domain. Variables at the outflow plane are set by extrapolation of properties from the interior grid.

Numerous studies have shown that the catalytic property of the Shuttle Orbiter thermal protection system (TPS) has an effect on surface heating that persists to approximately 160,000 ft. Thus a catalytic wall boundary condition has been included for this study. The implementation of this boundary condition is based on the work of Thompson[14] who assumed that only nitrogen and oxygen

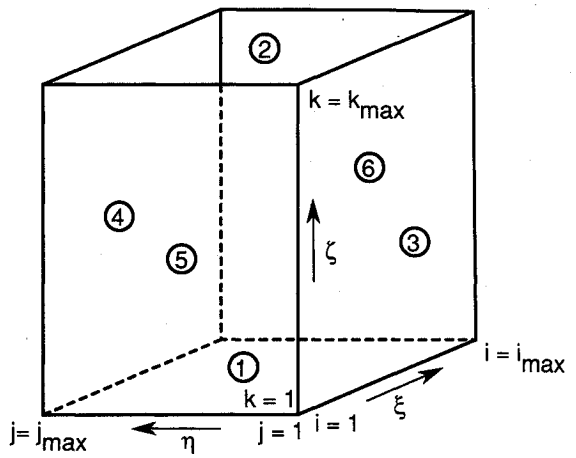

Fig. 7 Computational domain.

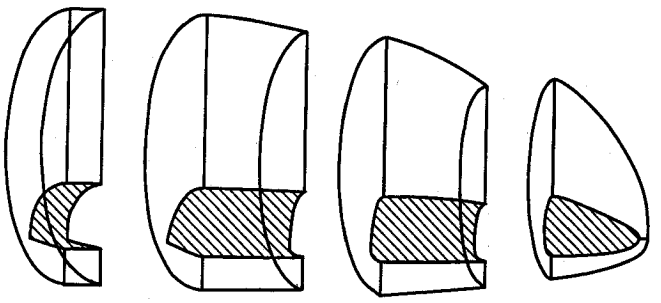

Fig. 8 Blocking structure for solution procedure.

recombine at the surface. Thompson also found that the best comparison with Shuttle flight data were obtained when Scott's[25] recombination rates for nitrogen and Zoby et al.'s[26] recombination rates for oxygen were used.

Computations presented herein take into account a variable wall temperature. The wall temperature is initially set at 1100 K and thereafter is based on the radiation equilibrium temperature at the wall; and, when determining these temperatures, the dependency of emissivity on temperature was taken into account.

Computational Domain

The computational domain for the solution is shown in Fig. 7. There are i_{max} points in the ξ direction, j_{max} points in the η direction, and k_{max} points in the ζ direction. Face 1 of the computational cube represents the vehicle surface and face 2 is the outer boundary. Faces 3 and 4 represent the leeside and windside symmetry planes, respectively. Face 6 is the outflow boundary and face 5 represents the line that connects the most forward point on the vehicle to the outer boundary.

Grid Block Structure

As stated in the Introduction, a global solution of the Navier-Stokes equations with nonequilibrium chemistry for the problem being considered here would far exceed the maximum CPU memory available to any one processor on current supercomputers. To overcome this limitation, a segmented solution approach is proposed for the problem. To accomplish this, the complete volume grid, shown in Fig. 5, is broken into separate blocks (Fig. 8), with the flowfield computation in each block treated as a stand-alone operation. To do this, the block boundaries cannot intersect any inviscid dominated flow regions with a subsonic axial flow component or any regions of axial flow separation. Previous experience with this configuration[27] at high angles of attack indicates a large region of subsonic flow at the nose and along the leading edge of the wing. For this solution, the volume grid has been divided into four blocks as shown in Fig. 8. The first block extends far enough downstream to encompass the subsonic flow in the nose region and extends to just aft of the canopy on the actual Orbiter vehicle. The second block terminates just before the wing-body intersection whereas the third block includes all of the wing leading edge. The fourth block contains the rest of the body and the outflow boundary. To minimize the effect of the outflow boundary on the continuing solutions, the upstream boundary for blocks two, three, and four is taken as the third plane of cells from the end of the block upstream of the block under consideration. The first block contains 44 axial planes. The second and third blocks contain 46 planes each, whereas the last block has 17 planes. All four blocks have 81 meridional planes and either 41 or 81 points between the surface and the outer boundary.

The size chosen for the blocks is governed not only by physical constraints, i.e., blocks one and three could not have an axial length less than that chosen here, but also by operational constraints. This problem could be addressed using only two blocks by combining block one with block two and block three with block four. However, few computers have the memory required for a two-block solution, and for those systems that have the needed memory, any routine access to it for any extended period of time is generally limited. Although limited by the physics of the flow, the segmenting approach provides a mechanism for efficiently and economically fitting a very large problem into any supercomputer operational environment.

Solution Technique

Block One

The solution in block one is started using the first block shown in Fig. 8. Freestream conditions are set at all the grid points except for those lying on the surface. There, the no-slip conditions are set along with either a constant wall temperature or a distribution of wall temperatures. The flowfield solution then evolves from that impulsive start. Once the bow shock structure is established, a subroutine within the LAURA code is called to align the grid to this shock shape by moving the outer boundary of the computational domain and redistributing points between the surface and outer boundary of the volume grid. This procedure allows the user to specify the number of points that lie in the freestream, thus maximizing the number of points that lie in the flowfield; and, since the shock is closely aligned with the grid, it is possible to maintain sharp shock profiles. The shock alignment procedure is called every 100 iterations until there is minimal movement in the grid. At the same time that the grid is being aligned with the shock, adjustments are made in the grid distribution at the wall to insure that the cell Reynolds number at the wall $N_{Re\text{-cell}}$ maintains a value 0(1). Grid adjustments are continued after the shock alignment is turned off to maintain resolution of the viscous layer as it develops and is discontinued as the solution approaches convergence.

To establish the surface temperature distribution, the initial wall temperatures are not updated until the solution is near convergence. Updated values of the radiation equilibrium temperature at the wall are determined from the relation

$$q_w = \sigma \varepsilon (T_w) T_w^4$$

where q_w is the current computed heating at the wall, and the dependence of emissivity on temperature is represented by curve fits of experimental data[27] for the shuttle TPS tiles. After the first iteration on the wall temperature and a return of the solution to near convergence, subsequent adjustments in the wall temperature had only a small effect on the rate of convergence of the solution. Three iterations on the wall temperature were usually sufficient to reduce the local relative change in the wall temperature to ± 5 K.

Additional Blocks

The solution procedure for each additional block is the same as outlined here for block two. Since the original block-one grid topology was altered by the grid adjustment that occurred during the block-one solution process, the original block-two grid cannot be used. A new initial grid for block two is created by interpolation from the original grid based on the plane in the converged block-one solution chosen as the upstream boundary for the new computation. The new grid for block two is first linearly interpolated

from the original grid. Then, the arclength distribution of points between the body and outer boundary in the block-one plane is imposed on the new grid. Thus, the newly created block-two grid does not match the original grid at the boundary between the two except at the wall and outer boundary. Figure 9 shows in the symmetry plane the converged block-one grid, the new initial block-two grid, and the remaining original grid. Only a few grid lines are shown for visual clarity. The new grid for block two is first linearly interpolated from the original grid. Then, the arclength distribution of points between the body and outer boundary in the block-one plane is imposed on the new grid. Thus, the newly created block-two grid does not match the original grid at the boundary between the two except at the wall and outer boundary. Although the arc length distribution from the last plane of block one is imposed on the subsequent volume grid, the arc length distribution over the rest of the body is sufficient to maintain a $N_{Re\text{-cell}}=0(1)$ on the windward surface.

The block-two flowfield is initialized by copying the solution from the plane in the first block chosen as the upstream boundary on to each plane of block two. Likewise, the wall temperatures from the upstream boundary are copied to each plane of block two. Starting from these conditions, the solution is carried out as in block one with one exception. When the grid adaption takes place, the outer boundary of the grid is allowed to move, but the relative distribution of points along grid lines lying between the wall and outer boundary found in the upstream boundary plane from block one is retained in each plane of block two. The resultant symmetry plane grid for converged solutions in block one and block two is shown in Fig. 10.

Solutions for the $k=81$ cases are started from the converged $k=41$ solutions. For these cases, the outer boundary of the volume grid is taken from the $k=41$ point solution and is frozen in that state. The grid doubling capability in the LAURA code is used to create a $k=81$ point grid along with a corresponding solution obtained by interpolation from the $k=41$ point case. In block one, the grid is allowed to evolve based on the $N_{Re\text{-cell}}=0(1)$ criteria. Once the block-one solution is converged, the arclength distribution of points between the surface and the outer boundary in block one is copied to the volume grid in the subsequent blocks.

Numerical Considerations

The effects of varying numerical parameters and formulations on the predicted heating levels have been studied. The number of cells in the k direction $k_{\max}$ extending from the body across the captured shock and into the freestream was set to 40 and 80. The

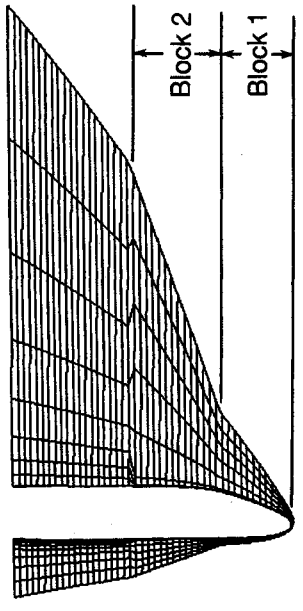

Fig. 9 Interpolated initial grid for block two.

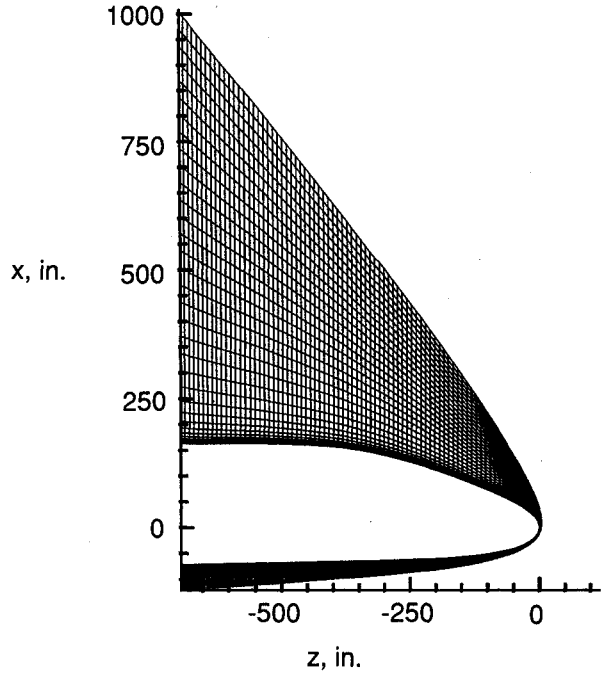

Fig. 10 Symmetry plane grid from converged solutions, block two.

limiter for the absolute value of eigenvalue in the k direction is scaled with the absolute value of the maximum eigenvalue using two different formulations. The formulation of the second-order-accurate, antidiffusive flux correction utilizing the min-mod function has been implemented in both a symmetric and upwind biased mode. Variation of these formulations and parameters typically lead to significant variation of predicted convective heating at the wall if the boundary layer is not adequately resolved.

The cell height at the wall is defined by specifying $N_{Re\text{-cell}}$ equal to 1.0. (A specification of $N_{Re\text{-cell}}=1.0$ is equivalent to defining the cell heights on the order of a mean free path because viscosity is approximately equal to the product of density, sound speed, and mean free path.) Therefore,

$$\Delta n_1 = N_{Re\text{-cell}} \left[\frac{\mu}{\rho a}\right]_{k=1} \tag{1}$$

where n is a running arclength along the ζ coordinate in the k direction, and μ the viscosity. A grid stretching factor f_k was used to control grid stretching from the wall across the boundary layer in the k direction. This parameter is defined by

$$f_k = \begin{cases} 1 + \mathrm{d}f_{\max} \sin\left\{\dfrac{2(k-1)\pi}{k_{\max}}\right\} & k \le \dfrac{k_{\max}}{2} \\ 1 & k \le \dfrac{k_{\max}}{2} \end{cases} \tag{2}$$

and

$$\mathrm{d}f_{\max} = \left\{\frac{n_{\max}}{2\Delta n_1}\right\}^{2/k_{\max}-1} \tag{3}$$

Therefore, cell height across the shock layer is defined by

$$\Delta n_{k+1} = f_k \Delta n_k \tag{4}$$

The value of $n_{\max}$ is periodically adjusted such that the captured shock location lies at $0.80 n_{\max}$. This specification places approximately half of the available points in the boundary layer in problems tested thus far. The remaining points span the distance from the boundary-layer edge to the inflow boundary in equal increments. The grid stretching factor is a maximum in the boundary layer at $k_{\max}/4$ and equals 1.716 and 1.310 for $k_{\max}$ equal to 40 and

80, respectively. The nondimensional grid distribution function n_k/n_{max} was calculated for the ζ coordinate line at $i=i_{max}$ and $j=j_{max}$ and imposed on all other ζ coordinate lines. Consequently, cell Reynolds numbers at the wall near the outflow boundary on the wind side are approximately equal to 1. (Recent updates allow the distribution to be calculated for each ζ coordinate line, but were not available for the present study.)

The m eigenvalues at generic cell face l, $\lambda_{l,m}$ of the inviscid flux Jacobian used in the determination of the upwind formulation are limited as follows:

$$\tilde{\lambda}_{l,m} = \begin{cases} |\lambda_{l,m}| & |\lambda_{l,m}| \geq 2\varepsilon \\ \dfrac{(\lambda_{l,m})^2}{4\varepsilon} + \varepsilon & |\lambda_{l,m}| \geq 2\varepsilon \end{cases} \tag{5}$$

The eigenvalue limiter ε was first used by Harten[22] to prevent the formation of expansion shocks across a sonic line where one eigenvalue equals zero. In the present formulation of the difference equations, its application is critical in blunt body flows to prevent instabilities, often in the form of reversed flows at the stagnation point, that occur in the stagnation region where the repeated eigenvalue U is near zero. Yee[29] introduced a scaling for ε based on the maximum eigenvalue. Radespiel and Swanson[28] suggested another scaling for ε based on the cell aspect ratio to minimize the dissipative effect of this parameter across a highly stretched boundary layer. Both of these scalings have been incorporated in the present work. Extensive tests with the LAURA code, some of which have been reported in Ref. 1, indicate that convective heating levels in the stagnation region of blunt body flows are relatively insensitive to the magnitude of ε applied in the k direction (across the boundary layer) if $f_k < 1.20$. However, the convective heating for flows with supersonic boundary-layer edge Mach numbers shows sensitivity to values of ε greater than 1% of the maximum eigenvlaue in the k direction. This sensitivity seems to be related to the importance of the shear work in defining the temperature profile across the boundary layer.

Because a significant portion of the STS flowfield has supersonic boundary-layer edge Mach numbers and because grid stretching factors are greater than 1.20, it is critical that the dissipative influence of ε be reduced as much as possible. To this end, the value of ε is defined by

$$\varepsilon = \varepsilon_0 (a_l + |U_l| + |V_l| + |W_l|) \tag{6}$$

where U, V, and W are the contraviant velocity components relative to cell face l, and the value of the scaling parameter ε_0 is defined by either

$$\begin{aligned} \varepsilon_0 &= 0.3 \\ &= 0.001 && k \text{ direction option 1} \\ &= 0.3 \min (1/AR^5, 1) && k \text{ direction option 2} \end{aligned} \tag{7}$$

Option 1 is the simplest to program but the solution is not sufficiently robust in leeside flow regions near the crossflow shock or in strong vortical flows near the leeside wingtip on Space Shuttle orbiter configurations. Option 2 forces the limiter to near zero values at the wall due to the high cell aspect ratios AR there but allows the limiter influence to ramp up to nominal values near the boundary-layer edge to provide greater solution robustness in difficult leeside regions. Options 1 and 2 are tested on the front part of the present configuration to assess the influence of the limiter on the surface heating.

The antidissipative flux correction for second-order accuracy is formulated in a symmetric mode with

$$S^{lim}_{l,m} = \min \text{mod} [2S_{l+1,m}, 2S_{l,m}, 2S_{l-1,m}, 1/2 (2S_{l-1,m} + 2S_{l+1,m})] \tag{8}$$

and in an upwind biased mode with

$$S^{lim}_{l,m} = D^+_{l,m} \min \text{mod} (S_{l-1,m}, S_{l,m}) + D^+_{l,m} \min \text{mod} (S_{l-1,m}, S_{l,m}) \tag{9}$$

where

$$D^{\pm}_{l,m} = 0.50 \left(1 \pm \frac{\lambda_{l,m}}{\tilde{\lambda}_{l,m}} \right) \tag{10}$$

The min-mod function returns the argument of smallest absolute magnitude when all of the arguments are of the same sign or returns zero if the arguments are of opposite sign. The symmetric limiter, derived by Yee,[23] does not yield a strictly upwind biasing on the formulation of the flux vector. The upwind limiter, following the form of Wang and Richards,[24] retains the proper zone of influence for the inviscid flux calculation and preliminary results indicate marginally better convergence rates than the symmetric limiter. Further details on the functional dependence of the of the flux formation on $S^{lim}_{l,m}$ may be found in Ref. 18.

Results and Discussion

The freestream conditions for the STS-3 flight (see Table 1) are used for the CFD computations. Two solutions have been obtained over the complete modified Orbiter model. The first was obtained using a 145×81×41 grid. The second, used to determine the effect of grid resolution in the k direction on the computed surface heat-

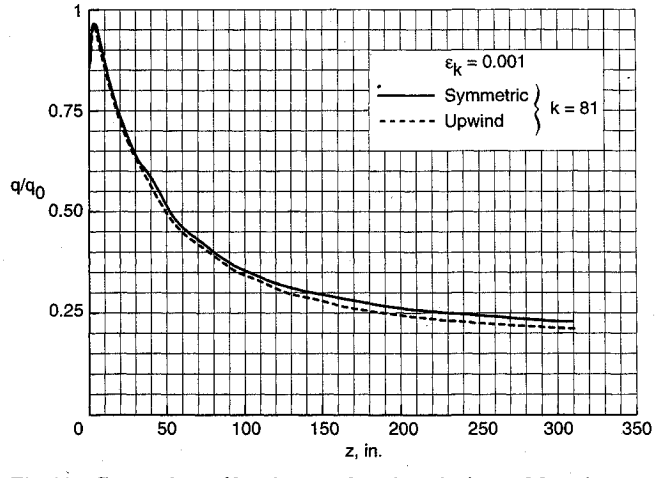

Fig. 11 Comparison of heating as a function of min-mod function at a constant grid density.

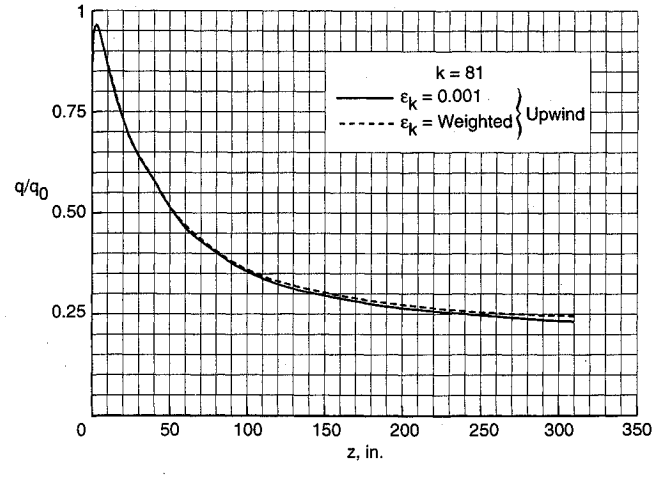

Fig. 12 Comparison of surface heating as a function of eigenvalue limiter at a constant grid density.

ing, was computed on a 145×81×81 grid. Each grid was broken up into four blocks consisting of 44, 46, 46, and 17 axial planes. The size of blocks two, three, and four allowed for overlap with each preceding block. For $k_{max}=41$, solutions for the largest blocks required approximately 40 CPU hours of CRAY-2 time along with 40 megawords of memory. Solutions for the $k_{max}=81$ cases required twice the memory but only about half the CPU time as the $k=41$ cases. The reduced CPU time for the $k_{max}=81$ cases was the result of the 81 point solution being initialized by interpolating from a converged $k=41$ point solution.

First, computations using only the first block will be used to illustrate the effect of different min-mod functions, eigenvalue limiters, and grid density on surface heating. Then, surface heating determined from $k=41$ and 81 point solutions will be compared with flight data over the complete lower surface of the modified Orbiter configuration.

In Fig. 11, the effect of min-mod function on the windward centerline surface heating is shown for the upwind and symmetric functions for a constant eigenvalue limiter and grid density. In the immediate nose region, there is virtually no difference in the two solutions whereas downstream the symmetric limiter produced a slightly lower surface heating than the upwind limiter. A comparison of surface heating on the centerline for the constant and aspect ratio weighted eigenvalue limiters for a grid density of 81 points in the k direction and an upwind min-mod function is shown in Fig. 12. Clearly, the choice of limiter has no effect on the surface heating. Finally, the effect of grid refinement on the surface heating using an upwind min-mod function and an aspect ratio weighed eigenvalue limiter is shown in Fig. 13. The high resolution solution produces an overall lower heating, but the difference is small. A comparison of the results from Figs. 11–13 shows that heating for all of the options falls within a 20% bandwidth at $z=200$ in.

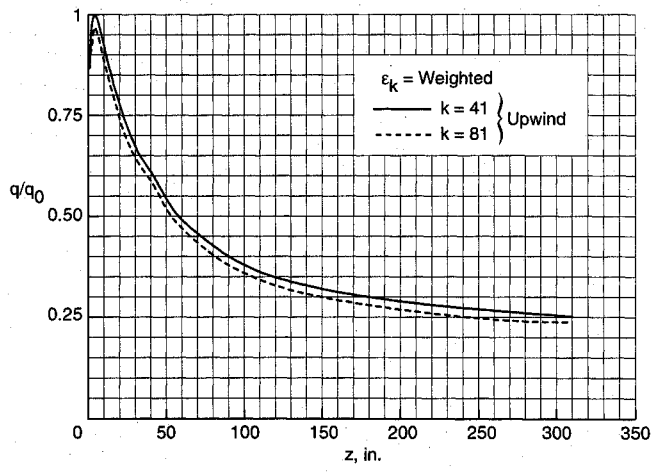

Fig. 13 Effect of grid resolution on surface heating for an upwind min-mod function and an aspect ratio weighted eigenvalue limiter.

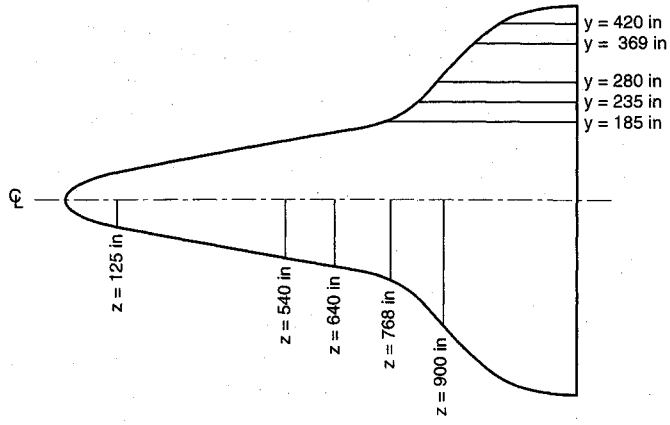

Fig. 14 Location of surface cuts for comparison of computed results and flight data.

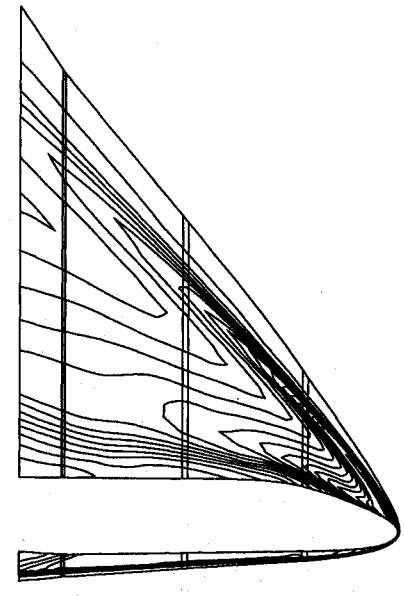

Fig. 15 Symmetry plane pressure contour plots for complete configurations, $k=41$.

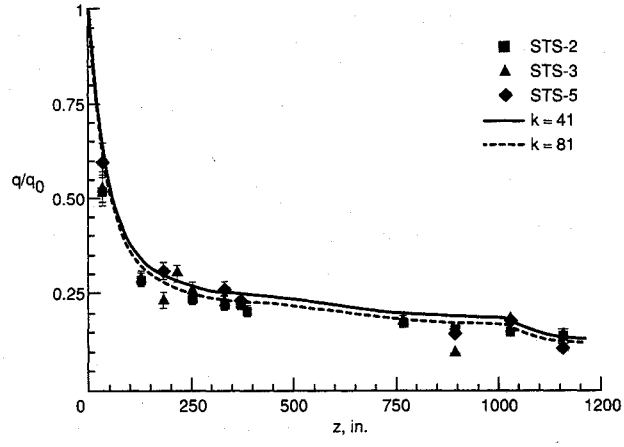

Fig. 16 Comparison of completed and measured windside centerline surface heating.

The comparison of computed results and flight data on a large geometrically complex vehicle like the Shuttle Orbiter must be tempered by an appreciation for the uncertainties associated with each data type. For the computation, the usual concerns about numerical accuracy must be taken into account. However, in this case, the accuracy of the chemistry, wall catalyticity, and surface emissivity models also become an issue. For the flight data, there are uncertainties other than those associated with the data reduction process. The data reduction process makes certain assumptions about the location of thermocouples within a thermal protection tile and assumes the gauge is in solid contact with the surface coating, neither of which is verifiable; and, that the gauges are correctly calibrated. In addition, the computational geometry is based on a mathematical representation of the design outer mold lines of the Orbiter and, by its very nature, that the mathematical model can very closely, but not exactly, reproduce the vehicle surface. On the other hand, there is no guarantee that the vehicle as flown conforms to the outer mold lines. With these issues in mind, a comparison of computer results and flight data is given in the following section of the paper.

The upwind min-mod limiter and the aspect ratio weighted eigenvalue limiter were chosen for computations over the com-

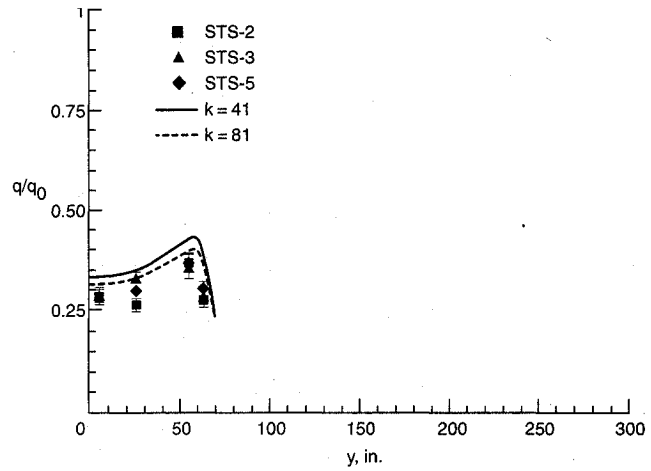

a) $z = 125$ in.

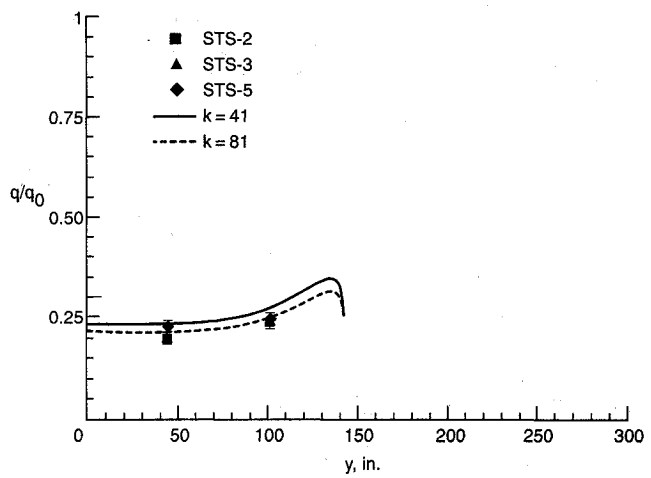

b) $z = 510$ in.

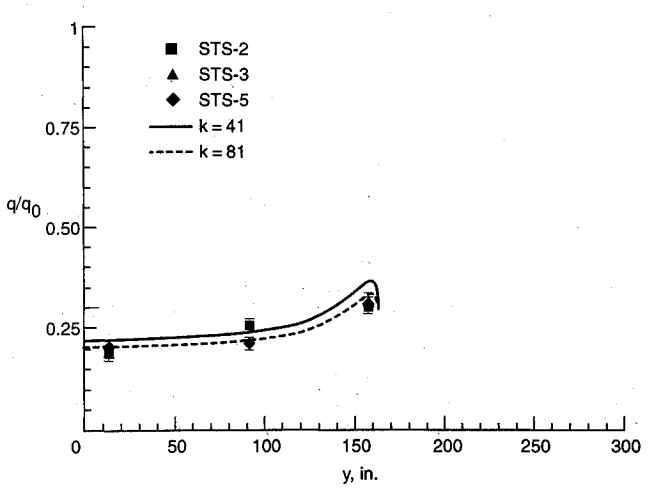

c) $z = 640$ in.

plete modified Orbiter configuration. The upwind min-mod limiter was chosen because, as already mentioned, it had exhibited somewhat better convergence characteristics than the symmetric limiter; and, as shown in Fig. 11, the choice of limiter had a very small effect on surface heating. Stability problems encountered on the aft portion of the leeside of the body forced the use of the aspect ratio weighted eigenvalue limiter. Computed results for $k=41$ and 81 are compared with the flight data from Shuttle flights two, three, and five at five axial locations along the body and at five outboard locations (Fig. 14) along the wing and along the windward centerline.

The quality of computed surface properties will be driven by the quality of the flowfield surrounding the configuration. Figure 15 shows a pressure contour plot in the upper and lower symmetry planes for the complete configuration. Also shown are the block boundaries and the domain overlap at each block face. This figure illustrates the smooth transition of the bow shock and flow in the shock layer across block boundaries.

Figure 16 shows the comparison of computed and measured heating along the windward centerline. The error bars on flight data represent an estimate of the possible error due only to the data reduction process that determines the wall heating. The computed results for both cases are in reasonable agreement with the flight

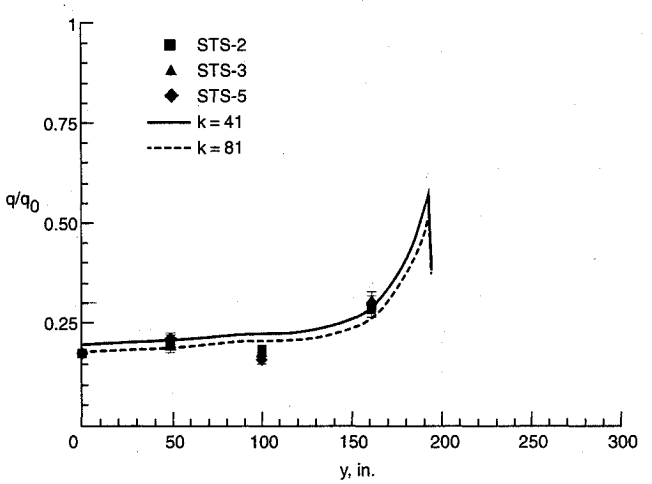

d) $z = 768$ in.

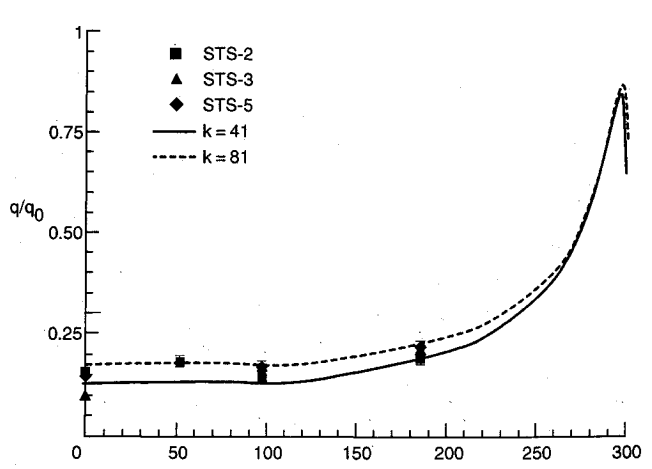

e) $z = 900$ in.

Fig. 17 Comparison of windside computed and measured circumferential surface heating distributions.

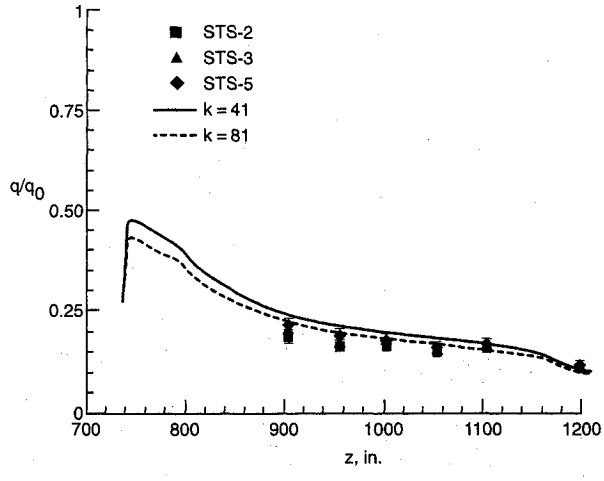

a) $y = 185$ in.

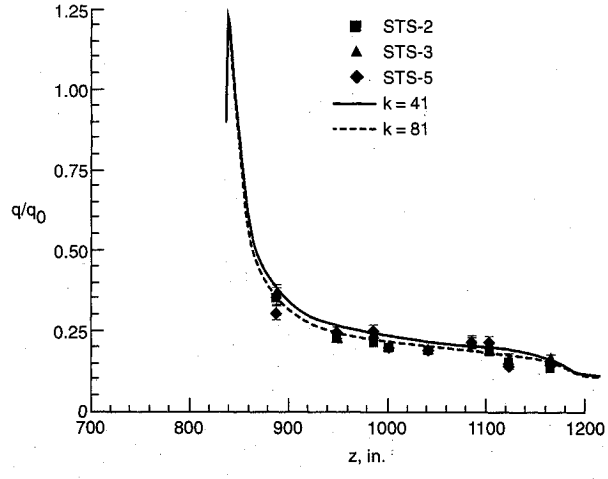

b) $y = 235$ in.

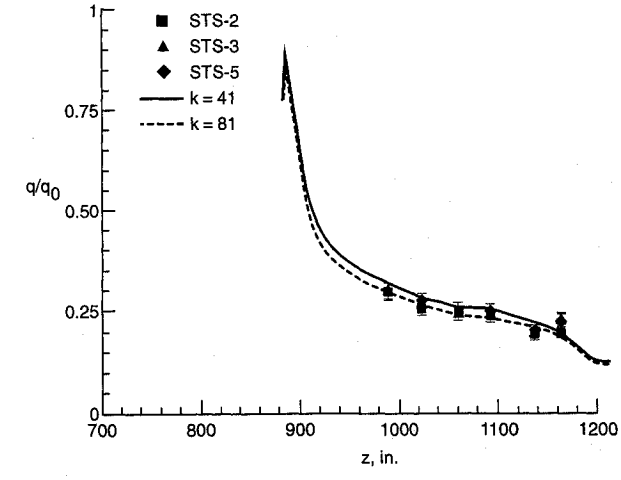

c) $y = 280$ in.

data even though it contains a lot of scatter. There is about a 10% difference between the high and low resolution cases and the high resolution solution appears to be a better representation of the trend of the flight data. Finding only a 10% difference in wall heating as the results of a doubling of grid resolution would indicate that the solution is, or very nearly is, grid converged. Also, there are no apparent discontinuities in the centerline wall heating distribution in the vicinity of the computational block boundaries.

Figures 17a–17e show the comparison of computed and measured heating at the five axial locations shown in Fig. 14. At the $z = 125$ in. cross section, Fig. 17a, the computational results overpredict the flight data. Although there is no apparent reason for this difference in computed and measured surface heating, it is most likely due to the computational surface not accurately representing the Shuttle surface in this region. For the other z stations, Figs. 17b–17e, the computed wall heating is in very good agreement with the limited amount of flight data. Again, the difference in heating between the two computed cases is about 10%; and, as before, the high resolution results are in better agreement with the flight data.

Figures 18a–18e show results for the comparison of computed and measured heating at wing chord locations as noted in Fig. 14. Although there is a reasonable distribution of thermocouple loca-

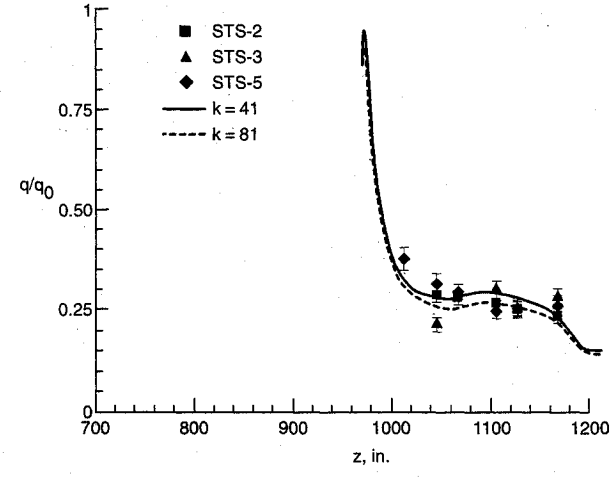

d) $y = 369$ in.

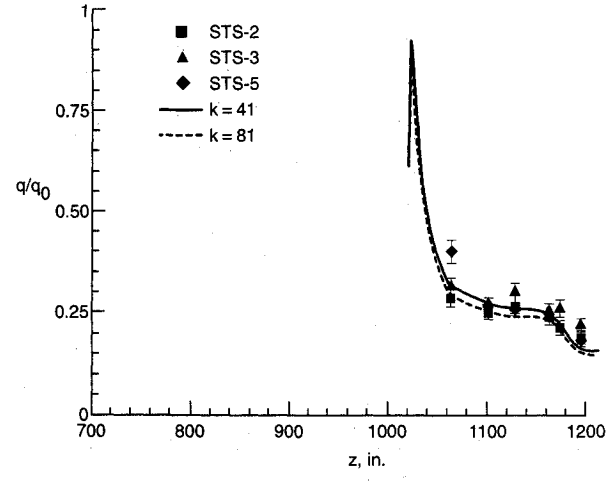

e) $y = 420$ in.

Fig. 18 Comparison of windside computed and measured circumferential surface heating distributions.

tions along each of the wing chords, there is no flight data in the vicinity of the wing leading edge where the gradient in the heating is the highest. In fact, the highest computed heating on the vehicle occurs at the wing leading edge at the wing chord location $y = 235$ in. There the heating is 25% higher than at the stagnation point. In Figs. 18b–18e, for values of z greater than 1150 in. (the location of the elevon hinge line), the flight data from STS-3 and STS-5 is slightly greater than that for STS-2 and the computed results. The surface definition model used in this study has the elevon deflection angle set at 0 deg. The elevons, which are slaved together during the hypersonic portion of re-entry, are set at -1.8 deg for STS-2, 3.7 deg for STS-3, and 1.7 deg for STS-5 where a positive angle indicates a rotation toward the windside of the vehicle. The flight data are consistent with the elevon settings and this difference in surface geometry accounts for the slight difference in the computed and measured heating in this region of the wing. The juncture between the third and fourth computational blocks occurs at $z = 1050$ in. in Figs. 18a–18e. As demonstrated earlier for the windward centerline, the transition from one block to the next does not adversely effect the heat transfer distribution.

The difference between the high and low resolution solutions is approximately 10% over the entire lower surface of the body. When the cell Reynolds number of 0(1) condition at the wall is implemented, it induces a severe stretching in the $k = 41$ grid near the wall. On the other hand, the $k = 081$ grid will have the same spacing at the wall, but twice as many points with which to fill the shock layer. This increased number of grid points allows the shock layer to be filled and still maintain a reasonable grid stretching at the wall. This difference in grid distribution at the wall is the primary reason for the difference in heating between the two solutions.

Conclusions

In this study, a procedure for computing the viscous flow over a modified Orbiter geometry at a hypersonic flight condition has been presented. The solutions, which focus on the windside of the configuration, model the flow as closely as possible through the inclusion of an appropriate thermochemical nonequilibrium chemistry model, a finite rate catalytic wall boundary condition, and wall temperature distributions based on radiation equilibrium temperatures at the wall. To reduce the memory requirement for this very large problem to a manageable level, a blocking procedure for the solution of the complete flowfield has been outlined; and, the computed results using this procedure show that it works very well. The investigation of the effect of different min-mod functions on the solution showed that the choice of min-mod function had a very small effect on the computed surface heating. The choice of eigenvalue limiter also had little effect on the surface heating. However, it was necessary to use the aspect ratio weighted limiter for the complete solution due to stability problems encountered on the leeside near the aft end of the configuration. Both the low and high resolution cases are in reasonable agreement with the flight data with the high resolution solution showing the better agreement with the trend of the flight data. Although reasonable values of wall heating have been obtained in this study using only 41 points between the wall and outer boundary of the grid, the issue of leeside flows has not been addressed. For vehicles such as the complete Orbiter at high angles of attack, the 81 points used for the high resolution case in this study may not be sufficient to resolve the flow on the leeside of the vehicle.

References

[1]Weilmuenster, K. J., and Hamilton, H. H., II, "A Comparison of Computer and Measured Aerodynamic Characteristics of a Proposed Aeroassist Flight Experiment Configuration," AIAA Paper 86-1366, June 1986.

[2]Weilmuenster, K. J., and Gnoffo, P. A., "Aeroassisted Flight Experiment Aerodynamic Characteristics at Flight Conditions," *Journal of Spacecraft and Rockets*, Vol. 27, No. 6, 1990, pp. 684–686.

[3]Hamilton, H. H., II, and Weilmuenster, K. J., "Calculation of Convective Heating on Proposed Aeroassist Flight Experiment Vehicle," AIAA Paper 86-1308, June 1986.

[4]Gnoffo, P. A., "Code Calibration Program in Support of the Aeroassist Flight Experiment," *Journal of Spacecraft and Rockets*, Vol. 27, No. 2, 1990, pp. 131–142.

[5]Weilmuenster, K. J., and Hamilton, H. H., II, "Comparison of Inviscid Flow Computations with Flight Data for the Shuttle Orbiter," *Journal of Spacecraft and Rockets*, Vol. 22, No. 3, 1985, pp. 297–303.

[6]Greene, F. A., Weilmuenster, K. J., and Micol, J. R., "Predicted Aerodynamics for a Proposed Personnel Launch Vehicle," AIAA Paper 90-1668, June 1990.

[7]Ma, E. C., Wey, T. C., and Li, C. P., "Flowfield Computations and Comparison with Shuttle Aerodynamic Data," AIAA Paper 91-1744, June 1991.

[8]Hamilton, H. H., II, Greene, F. A., and Weilmuenster, K. J., "Comparison of Heating Rate Calculations with Experimental Data on a Modified Shuttle Orbiter at Mach 6," AIAA Paper 91-1347, June 1991.

[9]Yamamoto, Y., "Numerical Simulation of Hypersonic Viscous Flow for the Design of H-II Orbiting Plane (HOPE)," AIAA Paper 91-1390, June 1991.

[10]Micol, J. R., "Aerothermodynamic Measurement and Prediction for Modified Orbiter at Mach 6 and 10," AIAA Paper 91-1436, June 1991.

[11]Vachris, A. F., and Yeager, L. S., "QUICK GEOMETRY—A Rapid Response Method for Mathematically Modeling Configuration Geometry," *Applications of Computer Graphics in Engineering*, NASA SP-390, 1975.

[12]Steinbrenner, J., Chawner, J., and Pouts, C., "Multiple Block Grid Generation in the Interactive Environment," AIAA Paper 90-1602, June 1990.

[13]Throckmorton, D. A., Hamilton, H. H., II, and Zoby, E. V., "Preliminary Analysis of STS-3 Entry Heat-Transfer Data for the Orbiter Windward Centerline," NASA TM-84500, June 1982.

[14]Thompson, R. A., "Comparison of Nonequilibrium Viscous-Shock-Layer Solutions with Shuttle Heating Measurements," *Journal of Thermophysics and Heat Transfer*, Vol. 4, No. 2, 1990, pp. 162–169.

[15]Hartung, L. C., and Throckmorton, D. A., "Space Shuttle Entry Heating Data Book. Vol. I— STS-2 (Parts 1 and 2)," NASA RP-1191, May 1988.

[16]Hartung, L. C., and Throckmorton, D. A., "Space Shuttle Entry Heating Data Book. Vol. II—STS-3 (Parts 1 and 2)," NASA RP-1191, May 1988.

[17]Hartung, L. C., and Throckmorton, D. A., "Space Shuttle Entry Heating Data Book. Vol. III —STS-5 (Parts 1 and 2)," NASA RP-1191, May 1988.

[18]Gnoffo, P. A., Gupta, R. N., and Shinn, J., "Conservation Equations and Physical Models for Hypersonic Air Flows in Thermal and Chemical Nonequilibrium," NASA TP-2867, Feb. 1989.

[19]Gnoffo, P. A., "Upwind-Biased, Point-Implicit Relaxation Strategies for Viscous Hypersonic Flows," AIAA Paper 89-1972, June 1989.

[20]Gnoffo, P. A., "An Upwind, Point-Implicit Relaxation Algorithm for Viscous, Compressible Perfect-Gas Flows," NASA TP 2953, Feb. 1990.

[21]Roe, P. L., "Approximate Riemann Solvers, Parameter Vectors, and Difference Schemes," *Journal of Computational Physics*, Vol. 43, No. 2, 1981, pp. 357–372.

[22]Harten, A., "High Resolution Schemes for Hyperbolic Conservation Laws," *Journal of Computational Physics*, Vol. 49, No. 3, 1983, pp. 357–393.

[23]Yee, H. C., "On Symmetric and Upwind TVD Schemes," NASA TM-86842, Sept. 1985.

[24]Wang, Z., and Richards, B. E., "High Resolution Schemes for Steady Flow Computation," *Journal of Computational Physics*, Vol. 79, No. 1, 1991, pp. 53–72.

[25]Scott, C. D., "Catalytic Recombination of Oxygen and Nitrogen in High-Temperature Reusable Surface Insulation," *Aerothermodynamics and Planetary Entry*, edited by A. L. Crosbie, Vol. 77, Progress in Astronautics and Aeronautics, AIAA, New York, 1981, pp. 192–212.

[26]Zoby, E. V., Gupta, R. N., and Simmonds, A. L., "Temperature Dependent Reaction Rate Expressions for Oxygen Recombination," *Thermal Design of Aeroassisted Orbital Transfer Vehicles*, edited by H. F. Nelson, Vol. 96, Progress in Astronautics and Aeronautics, AIAA, New York, 1985, pp. 445–465.

[27]Weilmeunster, K. J., and Hamilton, H. H., II, "Calculations of Inviscid Flow Over Shuttle-Like Vehicles at High Angles of Attack and Comparisons with Experimental Data," NASA TP-2103, May 1983.

[28]Radespiel, R., and Swanson, R. C., "Progress with Multigrid Schemes for Hypersonic Flow Problems," NASA CR 189579, Dec. 1991.

[29]Yee, H. C., Klopfer, G. H., and Montague, J. L., "High-Resolution Shock Capturing Schemes for Inviscid and Viscous Hypersonic Flows," NASA TM 100097, April 1988.